JOURNAL OF GEOPHYSICAL RESEARCH, VOL. 114, D12101, doi:10.1029/2008JD011472, 2009

Stratospheric gravity wave characteristics and seasonal variations observed by lidar at the South Pole and Rothera, Antarctica

Chihoko Yamashita,[1,2] Xinzhao Chu,[1] Han-Li Liu,[2] Patrick J. Espy,[3] Graeme J. Nott,[4] and Wentao Huang[1]

Received 14 November 2008; revised 18 February 2009; accepted 7 April 2009; published 17 June 2009.

[1] We present an observational study of stratospheric gravity wave spectra and seasonal variations of potential energy density at the South Pole (90°S) and Rothera (67.5°S, 68.0°W), Antarctica. The gravity wave spectra are derived from the atmospheric relative density perturbation in the altitude range of 30–45 km measured by an iron Boltzmann lidar. The ground-relative wave characteristics obtained at each location are comparable, with an annual mean vertical wavelength of ~4.1 km, vertical phase speed of ~0.7 m s^{-1}, and period of ~104 min. Approximately 44% of the observed waves show an upward phase progression while the rest display a downward phase progression in ground-based reference for both locations. Gravity wave potential energy density (GW-E_P) at Rothera is ~4 times higher than the South Pole in winter but is comparable in summer. Clear seasonal variations of GW-E_P are observed at Rothera with the winter average being 6 times larger than that of summer. The seasonal variations of GW-E_P at the South Pole are significantly smaller than those at Rothera. The absence of seasonal variations in wave sources and critical level filtering at the South Pole is likely to be responsible for the nearly constant GW-E_P. The minimum critical level filtering in winter at Rothera is likely to be a main cause for the winter enhanced GW-E_P, as this would allow more orography-generated waves to reach the 30 to 45 km range. The stratospheric jet streams may also contribute to the winter enhancement at Rothera.

Citation: Yamashita, C., X. Chu, H.-L. Liu, P. J. Espy, G. J. Nott, and W. Huang (2009), Stratospheric gravity wave characteristics and seasonal variations observed by lidar at the South Pole and Rothera, Antarctica, *J. Geophys. Res.*, *114*, D12101, doi:10.1029/2008JD011472.

1. Introduction

[2] Atmospheric gravity waves are a key element in defining large-scale circulation, thermal structure, chemical constituent distributions, and atmospheric variability from troposphere to thermosphere [*Fritts and Alexander*, 2003]. Poor representation of gravity waves in modern climate models is a leading source of uncertainty. Thus, improving the characterization of gravity wave spectra, propagation, dissipation, and source distributions is a very challenging and urgent issue for the atmospheric community. Numerous gravity wave observational techniques have been developed, and among them lidars provide high spatial/temporal resolutions and long-period observations to help address the issue. *Chanin and Hauchecorne* [1981] pioneered the lidar study of gravity waves. Following this, gravity waves were studied by lidars in the stratosphere and mesosphere at various midlatitude locations, e.g., Observatoire de Haute Provence (44°N, 6°E) and Biscarosse (44°N, 1°W) [*Wilson et al.*, 1991a, 1991b], Urbana (40°N, 88°W) [*Gardner et al.*, 1989; *Senft and Gardner*, 1991], and also in the Arctic [e.g., *Whiteway and Carswell*, 1994; *Gerrard et al.*, 2000]. Lidar studies of gravity waves in Antarctica are rare. *Collins and Gardner* [1995] pioneered a gravity wave study at the South Pole using a Na lidar to measure gravity waves in the Na density between 80 and 105 km, and in polar stratospheric clouds between 12 and 30 km. Observations of Antarctic gravity waves were also made by balloon radiosonde, satellite UARS/MLS, all-sky imager, MF radar, and GPS radio occultation [*Pfenninger et al.*, 1999; *Tsuda et al.*, 2000; *Hertzog et al.*, 2007, 2008; *Wu and Jiang*, 2002; *Espy et al.*, 2004, 2006; *Hibbins et al.*, 2007; *Baumgaertner and McDonald*, 2007]. However, most of these studies were either below 30 km or above 80 km, except two very recent reports by *Innis et al.* [2008] at Davis (68.6°S, 78°E) and *Chu et al.* [2009] at the South Pole and Rothera describing lidar studies of the correlation between polar mesospheric clouds and summer gravity waves in the 30 to 45 km range. Therefore, it is very valuable to obtain the missing piece of information for Antarctic gravity waves in between 30 and 80 km.

[1]Cooperative Institute for Research in Environmental Sciences and Department of Aerospace Engineering Sciences, University of Colorado at Boulder, Colorado, USA.
[2]High Altitude Observatory, National Center for Atmospheric Research, Boulder, Colorado, USA.
[3]Department of Physics, Norwegian University of Science and Technology, Trondheim, Norway.
[4]Department of Physics and Atmospheric Science, Dalhousie University, Halifax, Nova Scotia, Canada.

0148-0227/09/2008JD011472$09.00

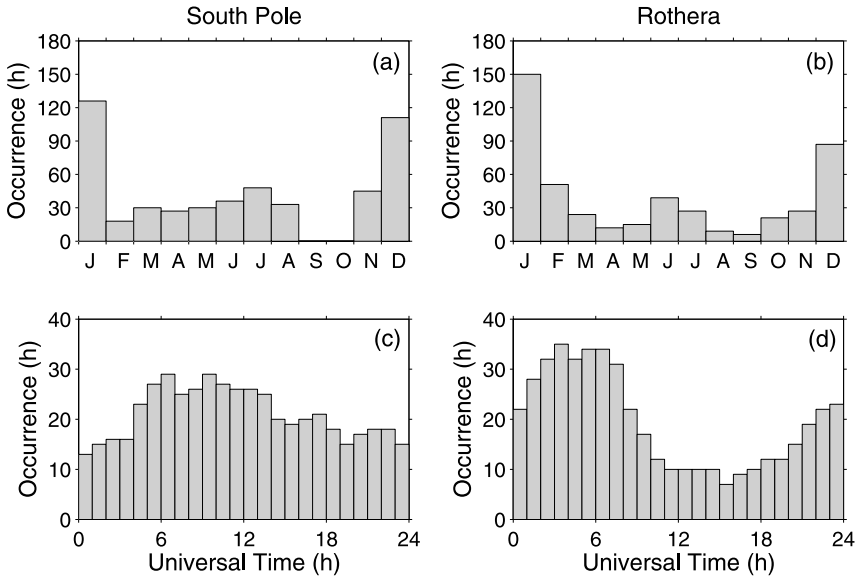

Figure 1. Histograms of the gravity wave occurrence hours versus month and universal time for the South Pole and Rothera. See text for details of lidar observations and examinations.

[3] The University of Illinois Fe Boltzmann lidar was operated at the South Pole (90°S) and then at Rothera (67.5°S, 68.0°W), Antarctica. Year-round atmospheric data at altitudes between 10 and 110 km were collected at both sites. Because this lidar functions as a Rayleigh lidar from 30 to 70 km and can provide atmospheric density data with high signal-to-noise ratios from 30 to 45 km, these data sets provide a unique opportunity to study stratospheric gravity waves and their seasonal variations at these two geophysically distinct locations. The Pole is on the Antarctic plateau while Rothera is on the western side of the Antarctic Peninsula surrounded by mountains and the Southern Ocean. Different wave features might be observed at these two sites because of different wave sources and the difference in their locations relative to the polar vortex that results in different propagation conditions. These observations therefore provide an opportunity to investigate wave sources, spectra, and propagation. In this paper we use the year-round data sets to characterize the stratospheric gravity wave spectrum, potential energy density and the seasonal variations in the altitude range between 30 and 45 km. Possible causes for the observed differences between the two sites are discussed in terms of potential differences in wave sources and critical level filtering.

2. Observations

[4] Gravity wave observations were made at the South Pole (90°S) from December 1999 to October 2001 and at Rothera (67.5°S, 68.0°W) from December 2002 to March 2005 using an Fe Boltzmann/Rayleigh lidar developed at the University of Illinois [*Chu et al.*, 2002]. Gravity waves are manifested as fluctuations in the atmospheric number density derived from the Rayleigh scattered signals. Pure Rayleigh signals exist from ~30 km (above aerosol layers) to 70 km (below the Fe fluorescence region). The signal-to-noise ratio (SNR) of lidar data decreases with height. For a 5-min integration and 192-m vertical resolution, the Fe Boltzmann lidar SNRs change from 62.6 at 30 km to 0.5 at 70 km. The altitude range of 30 to 45 km was chosen for its high SNR and also for comparison to the work of *Gerrard et al.* [1998].

[5] Lidar observations covered all 12 months throughout a year under both day and night conditions at the South Pole and Rothera. However, our data quality control removed the data in September and October for the South Pole because of the low Rayleigh counts and weather problems. Any data sets of less than 3 h were also excluded because of the use of a 3-h window in estimating the background density profile (see section 3). Hence, this gravity wave investigation covers 10 months of the year at the South Pole but all 12 months for Rothera, resulting in 618 and 507 observation hours respectively. Another criterion implemented to qualify the data as hours with gravity wave occurrence was that the RMS uncertainty of pure mean square relative density perturbation in the 3-h window had to be smaller than 50% of the perturbation itself [*Chu et al.*, 2009]. The total numbers of gravity wave occurrence hours are 507 h at the South Pole and 471 h at Rothera. Among these hours, 300 h and 318 h occur during summer (November to February), equaling 77% and 90% of the summer observations for the South Pole and Rothera, respectively. In winter (May to August), gravity waves occur during 150 h and 90 h, equating to 100% of the winter observations at both locations. The monthly and diurnal distributions of gravity wave occurrence hours are illustrated in Figure 1, where Rothera local midnight is 0430 UT. The larger database for wave examination during summer was primarily due to increased personnel and improved weather conditions. The reduction in the fraction of data meeting the wave criteria during summer and around noon at Rothera, is due to the additional solar background and the accompanying reduction in the signal-to-noise ratio.

3. Gravity Wave Spectral Analysis and Statistical Studies

[6] We characterize stratospheric gravity waves with an atmospheric relative density perturbation $r(z, t)$. The deri-

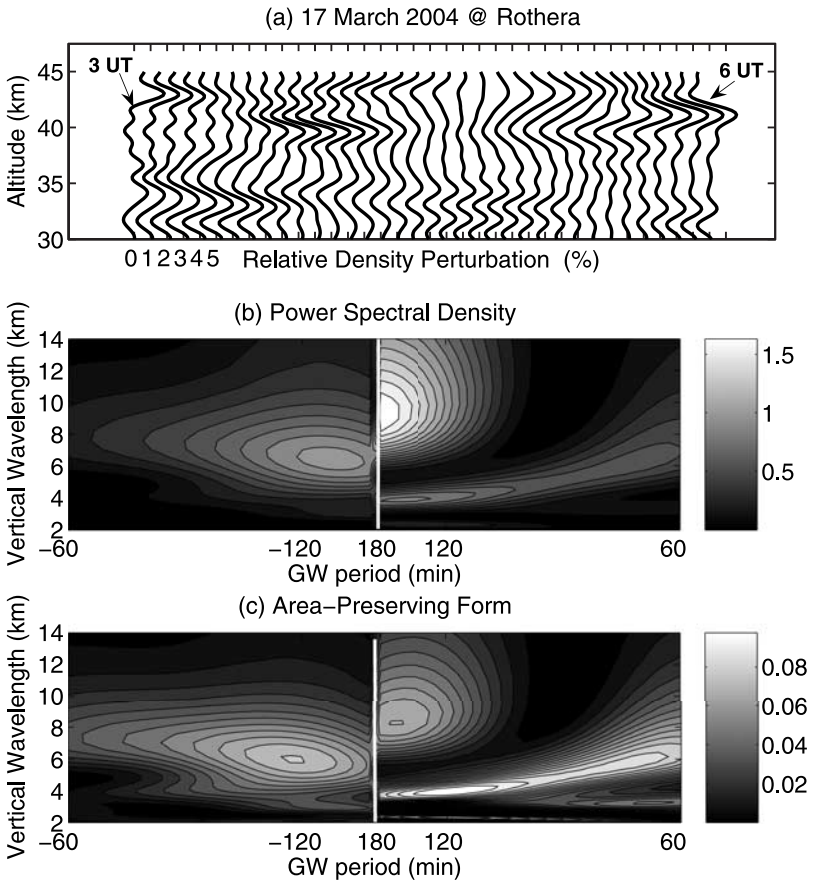

Figure 2. An example of spectral analysis (17 March 2004 at Rothera). (a) Sequence plot of relative density perturbation profiles. Each profile represents a 5-min data integration and it is shifted by 1% to the right progressively. (b) Power spectral density of the relative density perturbations shown in Figure 2a. (c) Area-preserving form of Figure 2b. Positive period represents downward phase progression.

vation of $r(z, t)$ from the lidar-obtained relative atmospheric density closely follows the approach taken by *Gardner et al.* [1989], *Hostetler and Gardner* [1990], and *Gerrard et al.* [2004]. Key points are summarized below. The $r(z, t)$ is defined as:

$$r(z,t) \equiv \frac{\rho'(z,t)}{\rho_0(z,t)} \equiv \frac{\rho(z,t) - \rho_0(z,t)}{\rho_0(z,t)} = \frac{\rho(z,t)/\rho(z_R,t) - \rho_0(z,t)/\rho(z_R,t)}{\rho_0(z,t)/\rho(z_R,t)}. \quad (1)$$

where $\rho(z_R, t)$ is the perturbed total atmospheric density at an altitude of z_R = 40 km for normalization purposes [*Gardner et al.*, 1989]. The quantity directly measured by the lidar is the perturbed total atmospheric density, $\rho(z, t)$, so we must estimate the background atmospheric density, $\rho_0(z, t)$, in order to derive the gravity wave-induced perturbation, $\rho'(z, t) \equiv \rho(z, t) - \rho_0(z, t)$. The background density $\rho_0(z, t)$ for gravity waves to propagate through is the atmosphere with the presence of tidal and planetary waves. These long-period waves should be preserved in the background estimation so that the obtained perturbation $\rho'(z, t)$ is purely due to small-scale gravity waves. In this study $\rho_0(z, t)$ is derived for each 3-h sliding window in the following steps similar to those of *Hostetler and Gardner* [1990] and *Gerrard et al.* [2004].

[7] 1. The perturbed relative density profiles $\rho(z, t)/\rho(z_R, t)$ in a 3-h window are averaged to remove waves with shorter temporal periods, while preserving the longer temporal-period waves as part of the 3-h averaged profile. According to *Kennedy* [1980], such an average is equivalent to a sinc filter with a 3-dB cutoff at 4.97 h for this 3-h window.

[8] 2. A 5th order polynomial fit with respect to altitude is applied to this profile to simulate the trend of the unperturbed background and long vertical wavelengths [*Shibata et al.*, 1986; *Mitchell et al.*, 1990]. This fit is used to detrend the data for the subsequent filtering operation. By subtracting the fit from the 3-h averaged profile, the residual obtained is a detrended 3-h averaged profile.

[9] 3. The residual profile is filtered to remove vertical variations with wavelengths shorter than 2 km. This reduces the high-frequency photon noise but retain long-period waves with vertical wavelengths longer than 2 km.

[10] 4. The 5th order polynomial trend is then added back to this filtered (detrended) residual to form the background relative density, $\rho_0(z, t)/\rho(z_R, t)$, for this 3-h window.

Table 1. Gravity Wave Propagation Direction in the 30–45 km at the South Pole and Rothera

	Number of Waves	Downward Phase Progression	Upward Phase Progression	Downward Phase to Total Wave Ratio
South Pole				
Total	471	264	207	56%
Summer	318	187	131	59%
Winter	91	46	44	51%
Rothera				
Total	501	279	222	56%
Summer	303	159	144	52%
Winter	150	93	57	62%

[11] This background relative density is therefore the sum of the unperturbed background density and perturbations induced by long-period waves (>5 h), such as tides and planetary waves. By subtracting $\rho_0(z, t)/\rho(z_R, t)$ from each 5-min $\rho(z, t)/\rho(z_R, t)$, these long-period waves are removed so the obtained relative density perturbation $r(z, t)$ given by equation (1) contains only the short temporal-period waves. To reduce photon noise in the perturbation profile, $r(z, t)$ is low-pass filtered to remove variations with vertical wavelengths shorter than 2 km and temporal periods shorter than 60 min. In the following spectral analysis, we only extract waves with periods between 1 and 3 h and vertical wavelengths between 2 and 15 km (window length) that dominate the relative density perturbation. Nevertheless, the potential energy density derived in section 4 will include contributions from waves with periods of ~1–6 h and vertical wavelengths of ~2–30 km (double the window length), as pointed out by *Senft and Gardner* [1991] and *Gerrard et al.* [2004].

[12] The resultant 2-D relative density perturbation $r(z, t)$ in the 3-h and 15-km window is then analyzed with a 2-D fast Fourier transform (FFT) method to reveal the wave spectrum. The power spectral density (PSD) for the data in Figure 2a is shown in Figure 2b. To identify the dominant waves, the PSD is converted to area-preserving form (Figure 2c), i.e., multiplying the PSD by the corresponding wave number and frequency following the approaches taken by *Smith et al.* [1987] and *Tsuda et al.* [2000]. The highest 1–3 peaks above the noise floor are then picked as the dominant waves. The vertical wavelengths λ_z and periods T of these waves are recorded and the corresponding vertical phase speeds are calculated as $c_z = \lambda_z/T$. As demonstrated by *Fukao et al.* [1985] and *Wilson et al.* [1991a], the 2-D FFT spectral analysis allows us to distinguish gravity wave propagation directions. Using the data shown in Figure 2 as an example, the two spectral peaks with positive periods correspond to downward phase progression waves while the peak with a negative period represents upward phase progression. It is worth pointing out that what is obtained from the lidar data is the ground-relative (apparent) frequency, not the intrinsic frequency.

[13] The above spectral analysis method is applied to each 3-h and 15-km data. The number of waves picked from each 3-h window is not fixed but varied between 1 and 3 peaks per data window. In Table 1 we summarize the total numbers of waves identified from the 3-h data windows and corresponding numbers of ground-relative downward and upward phase progression waves. The fractions of upward and downward phase-progression waves are calculated for the entire seasons as well as for the summer and winter seasons separately. Statistically, the downward phase-progression waves (positive frequencies) are 59% in summer but 51% in winter at the South Pole, and 52% in summer but 62% in winter at Rothera. The overall fractions of downward phase-progression waves in ground-based reference are 56% for both locations. Ground-based lidars observe the ground-relative frequency and phase speed, not intrinsic frequency or intrinsic phase speed. As pointed out by *Fritts and Chou* [1987] and *Fritts and Alexander* [2003], when the mean background wind is comparable to or larger than the intrinsic phase speed of the wave motion, the ground-relative frequency observed by the lidar can have an opposite sign of the intrinsic frequency, thus confusing the vertical directionality of the wave. Because of the lack of background wind and horizontal wave number information, we cannot firmly state the fractions of upward and downward propagating waves. Nevertheless, the ground-relative (apparent) phase progression information is still very valuable for comparison with model simulations. *Wilson et al.* [1991a] reported 65–80% of apparent downward phase progression for 30–50 km at 44°N, much larger than our results. This difference could be due to the different background wind conditions or the additional sources above our observational heights.

[14] We performed a statistical study on the spectra of both the upward and downward phase-progression waves identified above. Histograms of vertical wavelengths, vertical phase speeds, and periods of the dominant waves derived from the area-preserving form of each 3-h window are plotted in Figure 3 for both locations. The means, standard deviations, and standard errors of these spectral parameters are summarized in Tables 2 and 3 for the South Pole and Rothera, respectively. The overall statistics of gravity wave spectra are comparable between the South Pole and Rothera: the annual mean gravity wave vertical wavelengths are ~4.1 km, the vertical phase speeds ~0.7 m s^{-1}, and the periods ~104 min. There are no significant variations between the summer and winter seasons at either location considering the large standard deviations. Our observed vertical wavelengths are shorter than the previous results of 8–12 km observed by lidar between 30 and 45 km at Sondrestrom, Greenland (67°N, 310°E) [*Gerrard et al.*, 1998], and 8–10 km observed between 25 and 45 km by lidar at Eureka (80°N, 86°W) [*Whiteway and Carswell*, 1994]. Gravity waves between 35 and 50 km observed by lidar at Urbana (40°N, 88°W) showed two peaks of vertical wavelength at 2–4 km and 7–10 km [*Gardner et al.*, 1989]. Our histograms (Figure 3) also show a peak at ~2–4 km and then some longer wavelength waves that are comparable to Urbana results. The 3-km vertical wavelength between 18 and 35 km observed by CHAMP/GPS in Antarctica (60°S–90°S) [*Baumgaertner and McDonald*, 2007] is shorter than our results in the 30 to 45 km range. These differences could be due to the different observational filters of the respective measurement techniques. Our observed vertical phase speed of ~0.7 m s^{-1} is at the high end of previous observations: 0.01 to 0.85 m s^{-1} for Urbana and 0.55 to 0.83 m s^{-1} for Sondrestrom [*Gardner et al.*, 1989; *Gerrard et al.*, 1998]. The observed period of ~104 min in this study is slightly shorter but comparable

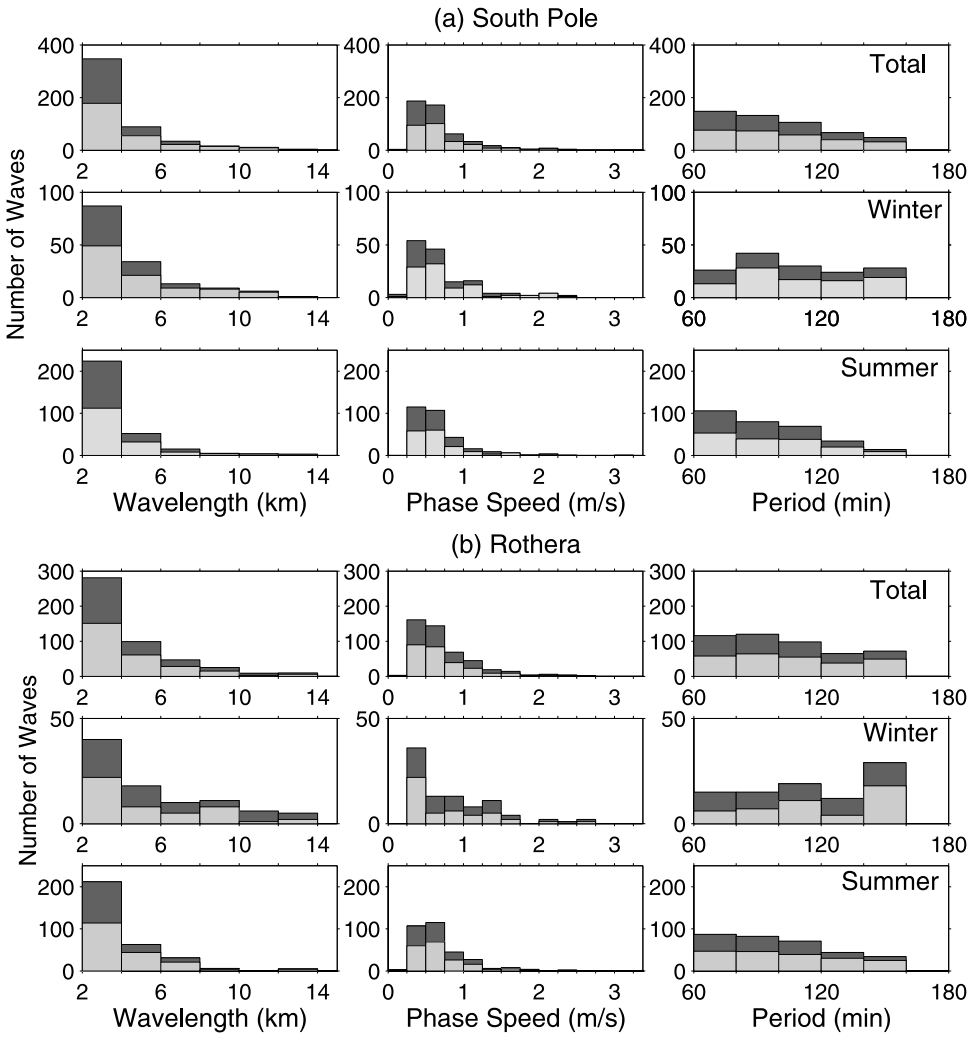

Figure 3. Spectra of the upward (darker histogram) and downward (lighter histogram) phase-progression gravity waves in the 30 to 45 km altitude range at (a) the South Pole and (b) Rothera: (top) entire season, (middle) winter (May to August), and (bottom) summer (November to February); (left) vertical wavelength, (middle) vertical phase speed, and (right) period.

Table 2. Gravity Wave Spectrum in the 30–45 km at the South Pole for Downward and Upward Phase Progression Waves

	Mean ± Standard Deviation (Standard Error)		
	Entire Season	Winter (May to Aug)	Summer (Nov to Feb)
Vertical wavelength (km)			
Downward	4.1 ± 2.2 (0.13)	4.8 ± 2.6 (0.27)	3.7 ± 1.8 (0.14)
Upward	3.6 ± 1.8 (0.12)	3.8 ± 1.9 (0.25)	3.6 ± 1.9 (0.16)
Vertical phase speed (m s^{-1})			
Downward	0.71 ± 0.41 (0.02)	0.77 ± 0.48 (0.05)	0.66 ± 0.34 (0.03)
Upward	0.66 ± 0.40 (0.03)	0.66 ± 0.42 (0.06)	0.68 ± 0.42 (0.04)
Period (min)			
Downward	102 ± 26 (1.5)	111 ± 28 (2.9)	97 ± 23 (1.9)
Upward	97 ± 25 (1.6)	108 ± 28 (3.7)	93 ± 22 (1.8)

Table 3. Gravity Wave Spectrum in the 30–45 km at Rothera for Downward and Upward Phase Progression Waves

	Mean ± Standard Deviation (Standard Error)		
	Entire Season	Winter (May to Aug)	Summer (Nov to Feb)
Vertical wavelength (km)			
Downward	4.4 ± 2.4 (0.15)	5.3 ± 3.0 (0.44)	4.1 ± 2.3 (0.15)
Upward	4.3 ± 2.4 (0.17)	5.6 ± 3.3 (0.50)	3.6 ± 1.7 (0.15)
Vertical phase speed (m s^{-1})			
Downward	0.73 ± 0.42 (0.03)	0.80 ± 0.53 (0.08)	0.70 ± 0.39 (0.03)
Upward	0.74 ± 0.44 (0.03)	0.88 ± 0.57 (0.09)	0.65 ± 0.32 (0.03)
Period (min)			
Downward	107 ± 28 (1.7)	120 ± 28 (4.2)	103 ± 27 (2.0)
Upward	101 ± 26 (1.8)	113 ± 30 (4.5)	98 ± 24 (2.1)

Table 4. Statistics of RMS Relative Density Perturbation at the South Pole and Rothera

	South Pole Mean ± Standard Deviation	Rothera Mean ± Standard Deviation
Entire Season	0.43 ± 0.17 (%)	0.52 ± 0.32 (%)
Winter (from May to Aug)	0.45 ± 0.12 (%)	0.95 ± 0.30 (%)
Summer (from Nov to Feb)	0.42 ± 0.18 (%)	0.37 ± 0.15 (%)
The ratio of winter to summer	1.07	2.51

to the periods of 120–180 min observed at Sondrestrom by *Gerrard et al.* [1998].

4. Gravity Wave Potential Energy Density and Its Seasonal Variations

[15] The mean potential energy density per unit mass $\overline{E_P}$ in the 2-D window of 3 h and 15 km is defined as:

$$\overline{E_P} = \overline{\frac{1}{2}\left(\frac{g}{N}\right)^2 \left\langle \left(\frac{\rho'(z,t)}{\rho_0(z)}\right)^2 \right\rangle} = \frac{1}{2}\overline{\left(\frac{g}{N}\right)^2}\langle r^2\rangle_{pure} \qquad (2)$$

where $\langle r^2\rangle_{pure} = \langle (r(z,t))^2\rangle - \overline{(\Delta r)^2}$ is the pure mean square (MS) relative density perturbation calculated for the 3-h and 30–45-km window with the positive bias due to photon noise, $\overline{(\Delta r)^2}$, removed [*Chu et al.*, 2009]. The gravitational acceleration is given by g, and N is the Brunt–Väisälä frequency as defined in [*Lighthill*, 1978]:

$$N^2 = -g\left(\frac{1}{\rho_0}\frac{d\rho_0}{dz} + \frac{g}{c_s^2}\right) = \frac{g}{T_0}\left(\frac{dT_0}{dz} + \frac{g}{C_p}\right), \qquad (3)$$

where c_s is the speed of sound and C_p is the specific heat at constant pressure. We take the first half of equation (3) to calculate the N^2 using the lidar-measured atmospheric number density: ρ_0 is the background density of the 3-h window as described above, and $d\rho_0$ is the background density difference between two altitude levels (dz = 1000 m). The sound speed, c_s, for an ideal gas is given by $c_s = \sqrt{\frac{C_p}{C_v}\frac{RT}{\mu}} = \sqrt{\frac{C_p}{C_v}R^*T}$, where R is the universal gas constant, μ is the atmosphere molecular weight, R^* is the gas constant of dry air (287.05 J kg^{-1} K^{-1}), C_p (1005 J kg^{-1} K^{-1}) and C_v (718 J kg^{-1} K^{-1}) are the specific heat at constant pressure and constant volume respectively, and T is the atmospheric temperature taken from the United Kingdom Met Office (UKMO) stratospheric assimilated data. The N^2 is calculated for each altitude and then $(g/N)^2$ is averaged over the 30 to 45 km range to obtain the mean $\overline{(g/N)^2}$. By scaling $\langle r^2\rangle_{pure}$ with $\overline{(g/N)^2}$, a mean potential energy density $\overline{E_P}$ is obtained for the 3-h and 30–45 km window using equation (2). Our approach described here is comparable to that of *Wilson et al.* [1991b] who used an averaged N^2 to scale the integrated power spectral density of density perturbation in selected spectrum range to derive the mean potential energy density.

[16] RMS relative density perturbations $(r)_{rms} = \sqrt{\langle r^2\rangle_{pure}}$ are calculated for each 3-h data window and the statistics of the results are given in Table 4. It is striking that Rothera RMS perturbations display a significant increase (over 2 times) from summer to winter while the South Pole RMS perturbations are nearly flat through the year. To illustrate the seasonal variations of RMS perturbations, we take the weekly means of these 3-h perturbations and then plot the weekly means against month in Figure 4a. Despite the large fluctuations, it is clear from Figure 4a that RMS perturbations are comparable between the South Pole and Rothera in summer but in winter Rothera RMS perturbations are much larger than those at the South Pole. The mean N^2 in each 2-D window of 30–45 km and 3 h is computed using equation (3) and then the weekly means of N^2 are plotted versus month in Figure 4b for both the South Pole and Rothera. From the RMS perturbations and N^2 obtained above, the mean gravity wave potential energy density per unit mass for each 3-h and 15-km window (GW-$\overline{E_P}$) is derived using equation (2) and the statistics of the results are summarized in Table 5. The

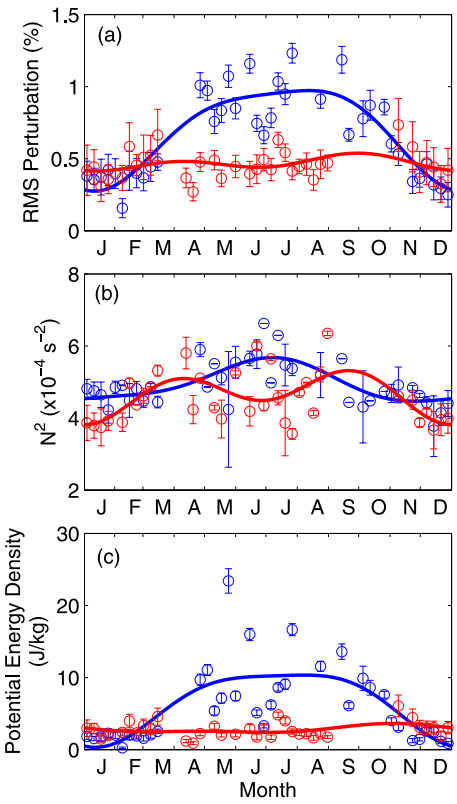

Figure 4. The seasonal variations of weekly mean (a) RMS relative density perturbation, (b) N^2, and (c) GW-$\overline{E_P}$ for the South Pole (red/gray) and Rothera (blue/black). The solid curves are the annual plus semiannual harmonic fittings given by equation (4). Error bars are the uncertainty of RMS relative density perturbation in Figure 4a, the standard deviations of N^2 in Figure 4b, and the uncertainty of GW-$\overline{E_P}$ in Figure 4c.

Table 5. Statistics of GW-$\overline{E_P}$ at the South Pole and Rothera

	South Pole Mean ± Standard Deviation	Rothera Mean ± Standard Deviation
Entire season	2.70 ± 2.11 (J kg^{-1})	4.21 ± 5.53 (J kg^{-1})
Winter (from May to Aug)	2.73 ± 1.91 (J kg^{-1})	10.97 ± 8.19 (J kg^{-1})
Summer (from Nov to Feb)	2.71 ± 2.18 (J kg^{-1})	1.80 ± 1.56 (J kg^{-1})
The ratio of winter to summer	1.00	6.61

Table 6. Fitting Curve Coefficients for RMS Relative Density Perturbations, N^2, and Gravity Wave Potential Energy Density at the South Pole and Rothera

	RMS (%)		N^2 ($\times 10^{-5}$ s^{-2})		GW-$\overline{E_P}$ (J kg^{-1})	
	South Pole	Rothera	South Pole	Rothera	South Pole	Rothera
A_{12}	0.04 ± 0.03	0.34 ± 0.03	3.54 ± 1.31	5.70 ± 0.97	0.54 ± 0.33	4.97 ± 0.83
Φ_{12} (day)	278 ± 28	197 ± 6	200 ± 32	180 ± 12	310 ± 28	196 ± 11
A_6	0.05 ± 0.03	0.08 ± 0.03	5.13 ± 1.83	1.59 ± 1.08	0.26 ± 0.29	1.23 ± 0.89
Φ_6 (day)	94 ± 15	98 ± 12	272 ± 8	195 ± 19	122 ± 35	101 ± 21
A_0	0.47 ± 0.02	0.69 ± 0.02	46.7 ± 1.2	49.6 ± 0.76	2.83 ± 0.22	6.51 ± 0.63
Correlation coefficient	29.9%	89.1%	59.1%	72.4%	32.9%	74.5%

potential energy density is similar between summer and winter at the South Pole while at Rothera, the potential energy density increases by about 6 times from summer to winter. The statistics also shows that the potential energy densities are comparable between the South Pole and Rothera in summer but in winter the Rothera potential energy density is about 4 times that of the South Pole. Weekly means of GW-$\overline{E_P}$ versus month are plotted in Figure 4c. The winter enhancement of GW-$\overline{E_P}$ is apparent at Rothera despite the large fluctuations.

[17] To help quantify the seasonal variations for both locations, the harmonic fits of "annual + semiannual + mean" given by equation (4) are applied to the weekly means of RMS perturbation, N^2, and GW-$\overline{E_P}$ shown in Figure 4:

$$y = A_{12}\cos\left[\frac{2\pi}{365}(x-\Phi_{12})\right] + A_6\cos\left[\frac{2\pi}{365/2}(x-\Phi_6)\right] + A_0, \quad (4)$$

where A_{12} and A_6 are amplitudes of annual (12 months) and semiannual (6 months) oscillations, Φ_{12} and Φ_6 are the corresponding phases, and A_0 is the annual mean. The obtained fitting parameters are summarized in Table 6. The RMS perturbation and GW-$\overline{E_P}$ at the South Pole are nearly constant and do not exhibit significant seasonal variations, although N^2 does show a weak seasonal dependence (>50% correlation). With balloon radiosonde data from 1993 to 1996, *Pfenninger et al.* [1999] reported a seasonal variation of gravity wave potential energy density in the 10 to 35 km range at the South Pole. They showed that potential energies vary between about 0.5 J kg^{-1} to 2.5 J kg^{-1} with a clear maximum in November from 11 to 35 km and a minimum in February from 11 to 21 km. The weak seasonal variations in the 30 to 45 km range, coupled with the large week-to-week variability, preclude our comparison to the observations by *Pfenninger et al.* [1999].

[18] The annual oscillations dominate the seasonal variations of RMS perturbation and GW-$\overline{E_P}$ at Rothera, with maxima around the day of year 196 to 197. The semiannual oscillation amplitudes are about one fourth those of the annual oscillations. Therefore, Rothera exhibits a clear seasonal trend with the maximum in winter and the minimum in summer. The GW-$\overline{E_P}$ seasonal variations observed at Rothera are comparable to observations made by others in Antarctica. MLS measurements showed the wave variance to be maximum in winter and minimum in summer around Drake Passage (50°S to 70°S latitude and 290°E to 315°E longitude) at ~28 km and ~43 km [*Wu and Jiang*, 2002]. *Baumgaertner and McDonald* [2007] reported Antarctic GW-$\overline{E_P}$ seasonal variations from ground to 35 km using CHAMP/GPS occultation temperature data. They took an average of the GW-$\overline{E_P}$ over the entire Antarctic (60°S to 90°S) and showed a peak of GW-$\overline{E_P}$ in August between 30 and 35 km. This is comparable to our results at Rothera, but different from those at the South Pole. The results of *Hertzog et al.* [2008] show that the wave momentum fluxes are generally larger from September to October than during December to January, but they exhibit a decrease in momentum flux as one approaches the pole. Similarly, gravity wave observations made with a MF radar at Rothera revealed a peak wind variance in winter in the mesosphere [*Hibbins et al.*, 2007]. Finally, lidar observations at Sondrestrom, Greenland (67°N, 310°E) exhibited the wave RMS perturbation in the 30 to 45 km range maximizing in winter and minimizing in summer [*Gerrard et al.*, 2000], very similar to the Rothera trend.

5. Discussion

[19] We discuss the possible causes for the observed different seasonal variations of GW-$\overline{E_P}$ at Rothera and the South Pole. There is an obvious difference in topography between the two sites: Rothera is surrounded by ocean and mountains while the South Pole is in the middle of the Antarctic plateau. In addition, Rothera is closer to the winter storm track that passes through the Drake Passage. Therefore, Rothera is expected to have much stronger gravity wave sources than the South Pole. *Baumgaertner and McDonald* [2007] observed strong GW-$\overline{E_P}$ between 18 and 27 km around the Antarctic Peninsula (~60°W) and the transantarctic mountains (~160°E) in the yearly average. Similarly, *Hertzog et al.* [2007, 2008] and *Ern et al.* [2004] also observed enhanced gravity wave activity below 30 km over the Antarctic Peninsula in winter. *Alexander and Teitelbaum* [2007] reported the propagation of a mountain wave from the troposphere to the stratosphere (above 30 km) over the Antarctic Peninsula. Similar mountain-wave propagation events were observed in the Vorcore campaign and simulated in the Weather Research and Forecast (WRF) model [*Plougonven et al.*, 2008]. *Espy et al.* [2006] observed a winter gravity wave momentum flux in the mesosphere that was four times larger at Rothera than at Halley station, which is well inland of the winter storm track and has a featureless topography like that of the South Pole. These results suggested that enhanced gravity wave sources could cause strong gravity wave activity near Rothera during the winter.

[20] Our results show the GW-$\overline{E_P}$ to be nearly equal during the summer at Rothera and the South Pole, but that it increases a factor of ~6 at Rothera during the winter. This is consistent with enhanced wave sources playing a greater

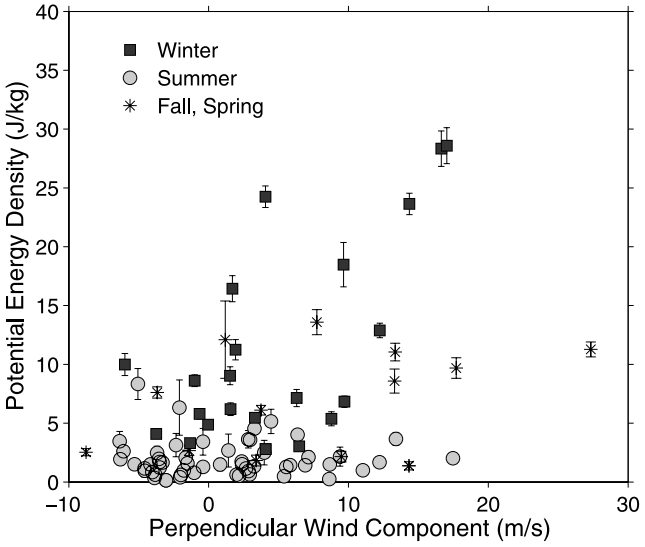

Figure 5. The correlation between daily mean background wind component perpendicular to the Antarctic Peninsula at ~3 km and GW-$\overline{E_P}$ at Rothera. Error bars are the uncertainty of GW-$\overline{E_P}$. Squares, circles, and asterisks represent data in winter (May–August), summer (November–February), and spring/fall, respectively.

role at Rothera during the winter in accordance with earlier studies. The wind component perpendicular to the Antarctic Peninsula derived from UKMO at a height of ~3 km over sea level, the approximate mountain height near Rothera, would allow us to account in both the wind amplitude and direction for the generation of orographic gravity waves. A correlation study between GW-$\overline{E_P}$ and the perpendicular wind component shows no significant correlation during the summer but a linear correlation coefficient of 65% (significant at the 99% level) during the winter at Rothera (Figure 5). This would indicate that orographic gravity waves are generated more during the winter at Rothera. However, while there may be a seasonal variation in the strength of orographically generated waves throughout the year, one must also consider the effects of critical level filtering on the observed GW-$\overline{E_P}$.

[21] Gravity waves can be filtered out by the background wind when the gravity wave horizontal phase velocity is equal to the background wind velocity [*Lindzen*, 1981; *Whiteway and Duck*, 1996; *Espy et al.*, 2004, 2006]. Seasonal variations of this critical level filtering effect can significantly influence the GW-$\overline{E_P}$ reaching the 30–45 km range. We examine the critical level filtering of both mountain waves and freely propagating waves. The critical level filtering effects on freely propagating gravity waves are examined with the wind-blocking diagram following *Taylor et al.* [1993]. We launch gravity waves from the mountain height with 0–40 m s^{-1} ground-based horizontal phase speed [*Garcia and Solomon*, 1985]. Assuming that the gravity wave propagation direction is homogeneously distributed from 0 to 360 degree and interpolating the UKMO wind data to fixed altitudes, we calculate the probability of upward propagating gravity waves reaching our observational range, i.e., the transmission of gravity waves through the lower atmosphere. The results of such probability versus altitude and month are illustrated in Figure 6b for Rothera. The mean probability of reaching 30–45 km (Figure 6a) is between 70% and 80% for summer months but around 55% during winter. This indicates that

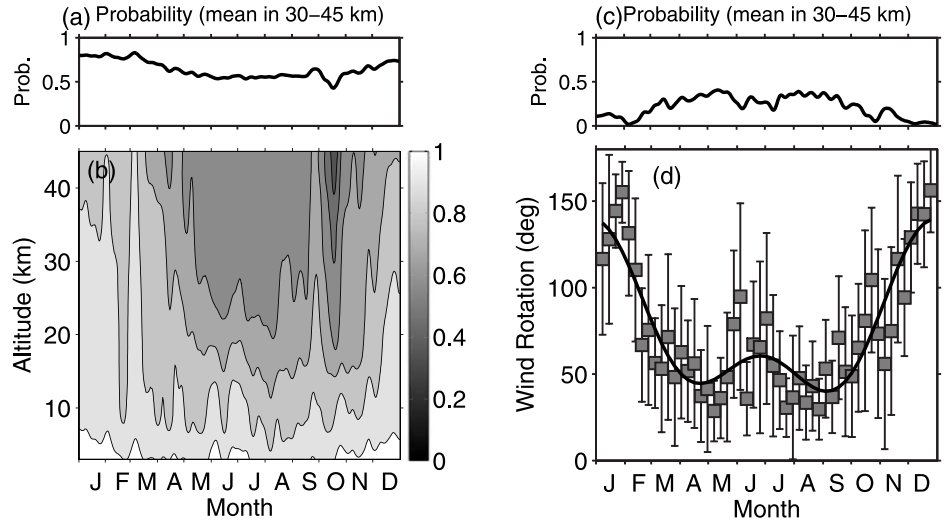

Figure 6. (a) The mean probability for freely propagating gravity waves reaching our observational heights between 30 and 45 km. (b) Seasonal variations of the probability for freely propagating gravity waves to reach each altitude at Rothera in 2003 and 2004, assuming that gravity wave propagation directions are distributed homogeneously from 0 to 360 degrees, and the phase speeds are 0–40 m s^{-1}. A 15-day Hamming window is used to smooth the contour. (c) The mean probability similar to Figure 6a but for mountain waves with phase speeds of 0–1 m s^{-1}. (d) Seasonal variations of weekly mean wind rotations from 3 to 30 km at Rothera. Weekly means are calculated with the UK Met Office data from December 2002 to March 2005. Error bars are $\pm 1\sigma$. The solid curve is the annual plus semiannual harmonic fit.

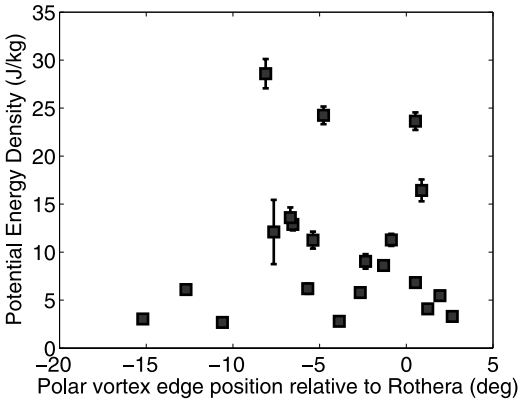

Figure 7. Correlations between the GW-$\overline{E_P}$ and the locations of polar vortex edge relative to Rothera. Zero degree means that polar vortex edge is at Rothera, negative degrees mean that Rothera is inside the vortex toward the pole, and positive degrees mean that Rothera is outside the vortex. Each data point of GW-$\overline{E_P}$ is daily mean, and each data point of polar vortex position is calculated from daily National Centers for Environmental Prediction reanalysis data.

freely propagating gravity waves can contribute to our observed GW-$\overline{E_P}$ through a year but their chances to reach the observational heights are more in summer than in winter at Rothera.

[22] With similar wind-blocking diagram we calculate the mean probability of mountain waves to reach the 30–45 km range. This is done by launching waves with phase speeds of 0–1 m s^{-1}. The obtained results in Figure 6c indicate that mountains waves have higher probability to reach our observational height in winter (~50%) than in summer (nearly zero). Following *Baumgaertner and McDonald* [2007], we derived the wind rotation using UKMO wind data, which is defined as the maximum wind direction change from the mountain height (~3 km) to 30 km. The weekly averaged wind rotations obtained at Rothera are plotted in Figure 6d. Significant wind rotations (>90°) occur in summer with significantly smaller wind rotations in winter. As suggested by *Whiteway and Duck* [1996] and *Baumgaertner and McDonald* [2007], wind rotations >90° in the lower atmosphere imply critical level filtering of the mountain waves. Figure 6d indicates that mountain waves have very little chance of reaching our observational heights in summer at Rothera but much higher probabilities in winter, consistent with the wind-blocking diagram results. Hence, even a constant source of mountain waves would have a larger contribution to our observed GW-$\overline{E_P}$ in winter than in summer at Rothera. No clear seasonal variations of the critical level filtering are found in either the wind rotation or the blocking diagram for the South Pole. It is likely that neither the critical level filtering nor the wave source has significant seasonal variations at the South Pole, which is consistent with the nearly constant GW-$\overline{E_P}$ observed through a year.

[23] The seasonal variations of the critical level filtering effects at Rothera may help explain our observations. Although orographic sources at Rothera are much stronger than at the South Pole, the strong critical level filtering effects in summer remove most mountain waves but allow most freely propagating waves to reach the 30 to 45 km range. As the freely propagating waves are not significantly filtered at either Rothera or the South Pole, there is a comparable GW-$\overline{E_P}$ between the two sites in summer. However, in winter most mountain waves at Rothera can propagate upward to reach our observational heights, leading to much higher winter GW-$\overline{E_P}$ at Rothera than at the South Pole. This situation also enables us to observe the positive correlation between the surface perpendicular wind component and the GW-$\overline{E_P}$ in winter at Rothera, and the large fluctuations in winter GW-$\overline{E_P}$. Although freely propagating waves are more heavily filtered during the winter at Rothera, one cannot exclude the possibility that sources of these waves increase at Rothera while remaining relatively constant at the South Pole, since the measurements of GW-$\overline{E_P}$ do not distinguish the two types of waves.

[24] The wintertime polar vortex may contribute to the GW-$\overline{E_P}$ enhancement in winter at Rothera. To examine the polar vortex effects, the polar vortex edge position relative to Rothera is calculated using National Centers for Environmental Prediction reanalysis data, and the results are shown in Figure 7 along with the GW-$\overline{E_P}$. No statistically significant correlation exists between vortex position and GW-$\overline{E_P}$ at Rothera; however, all of the large GW-$\overline{E_P}$ (>10 J kg^{-1}) events are observed between +5 and −10 degrees from the vortex edge, and no large GW-$\overline{E_P}$ is observed outside 10 degrees. This result is consistent with the previous CHAMP/GPS observations of the gravity wave enhancement within ±10 degrees from the vortex edge [*Baumgaertner and McDonald*, 2007]. *Whiteway et al.* [1997] suggested two reasons of gravity wave enhancement by polar vortex: a reduction of the critical level filtering effects and the Doppler shift of vertical wavelength. Gravity wave generation by the polar vortex through the geostrophic adjustment has also been suggested [*Yoshiki et al.*, 2004; *O'Sullivan and Dunkerton*, 1995; *Zhang*, 2004].

[25] The spectral analysis results in section 3 show ~44% waves having apparent upward phase progression at both the South Pole and Rothera. This percentage is much larger than the previous observations like those of *Wilson et al.* [1991a]. It is necessary to point out that if the background wind flowing over the mountains varies in time, it may cause the mountain waves appearing as upward (or downward) phase progression in the perturbation profiles at Rothera, although the waves in this case are propagating upwards. However, we observed similar percentage at the South Pole where the mountain waves are believed to be absent. In addition, *Pfenninger et al.* [1999] did not find correlations between tropospheric and stratospheric gravity wave spectra at the South Pole, and 20% of their observed waves in the 16 to 23 km region propagated downward. They suggested that there were wave sources above their observed altitudes, resulting in gravity wave spectrum varying with altitude. At Syowa (69°S, 39°E), *Yoshiki et al.* [2004] observed from radiosonde data that ~43% waves in the range of 15–25 km propagated downward in winter while ~12% downward propagating waves in summer. Considering all these results, we speculate that some of our observed waves with apparent upward phase progression might represent downward energy propagation. Since

our observational range at Rothera is located near the edge of the polar vortex, this stratospheric jet stream may have contributed to the downward propagating waves, as suggested by *Sato and Yoshiki* [2008] for Syowa. Regarding the summer case at Rothera and for the South Pole case, other sources or waves reflected by the region of evanescence above our observational heights could be responsible. Such downward propagating waves and causes deserve further investigation but are beyond the scope of this work.

6. Conclusions

[26] We present the first observational study of stratospheric gravity wave spectra, potential energy density, and seasonal variations through an entire year in the 30 to 45 km region at Antarctica with an Fe Boltzmann/Rayleigh lidar data. Our data analysis approach reliably extracts gravity wave spectra with vertical wavelengths of 2–15 km and periods of 60–180 min. The obtained ground-relative gravity wave spectra are comparable between the South Pole and Rothera: the annual mean gravity wave vertical wavelength is ∼4.1 km, the vertical phase speed ∼0.7 m s^{-1}, and the period ∼104 min. The observed ground-based gravity waves are dominated by waves with downward phase progression but ∼44% waves show upward phase progression at both sites. However, because of Doppler shift effects, these ground-relative upward phase speeds do not necessarily represent downward energy propagation. The observed GW-$\overline{E_P}$ in the 30 to 45 km region are comparable between Rothera and the South Pole in summer (∼1.8–2.7 J kg^{-1}), but the winter GW-$\overline{E_P}$ at Rothera (∼11 J kg^{-1}) is about 4 times larger than that at the South Pole. The observed Rothera GW-$\overline{E_P}$ shows a significant seasonal variation with the winter average being 6 times larger than the summer values. The seasonal variations of GW-$\overline{E_P}$ at the South Pole are much weaker than those at Rothera, with nearly constant values (∼2.7 J kg^{-1}) through the year.

[27] Our investigations suggest that the critical level filtering of orographic gravity waves may have played a key role in the GW-$\overline{E_P}$ seasonal variations at Rothera. Even though the wave sources are expected to be much stronger at Rothera, the strong critical level filtering effect in summer removes most mountain waves, resulting in comparable GW-$\overline{E_P}$ between these two locations. The minimum critical level filtering in winter allows most orographic gravity waves to propagate upward and reach the 30–45 km range, leading to the winter wave enhancement at Rothera. The polar vortex may also contribute to the Rothera GW-$\overline{E_P}$ enhancement in winter. The absence of clear seasonal variations in wave sources and critical level filtering is likely responsible for the significantly small seasonal variations of GW-$\overline{E_P}$ observed at the South Pole. We speculate that the polar vortex may act as a source for downward propagating waves in the wintertime at Rothera, and waves reflected from the region of evanescence above our observational heights might introduce waves propagating downward in summer or at the South Pole. The downward propagating waves and the South Pole seasonal variations certainly deserve further investigation with more observational data and gravity wave modeling.

[28] **Acknowledgments.** We sincerely acknowledge Jan C. Diettrich and the staff of the British Antarctic Survey for their operation of the lidar at Rothera. We also acknowledge two winter-over scientists, Ashraf El Dakrouri and John Bird, and the staff of Amundsen-Scott South Pole Station for their help and support in collecting data at the South Pole. We appreciate the valuable discussion with Dave Fritts. Rothera lidar project was supported by the U.K. Natural Environmental Research Council and by the United States National Science Foundation. C.Y., X.C., and W.H. were partially supported by NSF grants ATM-0602334, ATM-0645584, ATM-0632501, and ATM-0545353. C.Y. sincerely acknowledges the generous support of NCAR Newkirk Graduate Fellowship. H.L.L's effort is in part supported by the Office of Naval Research (N00014-07-C0209). National Center for Atmospheric Research is sponsored by the National Science Foundation.

References

Alexander, M. J., and H. Teitelbaum (2007), Observation and analysis of a large amplitude mountain wave event over the Antarctic peninsula, *J. Geophys. Res.*, *112*, D21103, doi:10.1029/2006JD008368.

Baumgaertner, A. J. G., and A. J. McDonald (2007), A gravity wave climatology for Antarctica compiled from Challenging Minisatellite Payload/Global Positioning System (CHAMP/GPS) radio occultations, *J. Geophys. Res.*, *112*, D05103, doi:10.1029/2006JD007504.

Chanin, M.-L., and A. Hauchecorne (1981), Lidar observations of gravity and tidal waves in the stratosphere and mesosphere, *J. Geophys. Res.*, *86*, 9715–9721, doi:10.1029/JC086iC10p09715.

Chu, X., W. Pan, G. Papen, C. S. Gardner, and J. Gelbwachs (2002), Fe Boltzman temperature lidar: Design, error analysis, and initial results at the North and South Pole, *Appl. Opt.*, *41*, 4400–4410, doi:10.1364/AO.41.004400.

Chu, X., C. Yamashita, P. J. Espy, G. J. Nott, E. J. Jensen, H.-L. Liu, W. Huang, and J. P. Thayer (2009), Responses of polar mesospheric cloud brightness to stratospheric gravity waves at the South Pole and Rothera, Antarctica, *J. Atmos. Sol. Terr. Phys.*, *71*, 434–445, doi:10.1016/j.jastp.2008.10.002.

Collins, R. L., and C. S. Gardner (1995), Gravity wave activity in the stratosphere and mesosphere at the South Pole, *Adv. Space Res.*, *16*, 81–90, doi:10.1016/0273-1177(95)00175-E.

Ern, M., P. Preusse, M. J. Alexander, and C. D. Warner (2004), Absolute values of gravity wave momentum flux derived from satellite data, *J. Geophys. Res.*, *109*, D20103, doi:10.1029/2004JD004752.

Espy, P. J., G. O. L. Jones, G. R. Swenson, J. Tang, and M. J. Taylor (2004), Seasonal variations of the gravity wave momentum flux in the Antarctic mesosphere and lower thermosphere, *J. Geophys. Res.*, *109*, D23109, doi:10.1029/2003JD004446.

Espy, P. J., R. E. Hibbins, G. R. Swenson, J. Tang, M. J. Taylor, D. M. Riggin, and D. C. Fritts (2006), Regional variations of mesospheric gravity wave momentum flux over Antarctica, *Ann. Geophys.*, *24*, 81–88.

Fritts, D. C., and M. J. Alexander (2003), Gravity wave dynamics and effects in the middle atmosphere, *Rev. Geophys.*, *41*(1), 1003, doi:10.1029/2001RG000106.

Fritts, D. C., and H.-G. Chou (1987), An investigation of the vertical wave number and frequency spectra of gravity wave motions in the lower stratosphere, *J. Atmos. Sci.*, *44*, 3610–3624.

Fukao, S., Y. Maekawa, T. Sato, and S. Kato (1985), Fine structure in mesospheric wind fluctuations observed by the Arecibo UHF Doppler radar, *J. Geophys. Res.*, *90*, 7547–7556, doi:10.1029/JA090iA08p07547.

Garcia, R. R., and S. Solomon (1985), The effect of breaking gravity waves on the dynamics and chemical composition of the mesosphere and lower thermosphere, *J. Geophys. Res.*, *90*, 3850–3868, doi:10.1029/JD090iD02p03850.

Gardner, C. S., M. S. Miller, and C. H. Liu (1989), Rayleigh lidar observations of gravity wave activity in the upper stratosphere at Urbana, Illinois, *J. Atmos. Sci.*, *46*, 1838–1854, doi:10.1175/1520-0469(1989)046<1838:RLOOGW>2.0.CO;2.

Gerrard, A. J., T. J. Kane, and J. P. Thayer (1998), Noctilucent clouds and wave dynamics: Observations at Sondrestrom, Greenland, *Geophys. Res. Lett.*, *25*, 2817–2820, doi:10.1029/98GL02107.

Gerrard, A. J., T. J. Kane, and J. P. Thayer (2000), Year-round temperature and wave measurements of the Arctic middle Atmosphere for 1995–1998, *Geophys. Monogr.*, *123*(22), 213–219.

Gerrard, A. J., T. J. Kane, J. P. Thayer, and S. D. Eckermann (2004), Concerning the upper stratospheric gravity wave and mesospheric cloud relationship over Sondrestrom, Greenland, *J. Atmos. Sol. Terr. Phys.*, *66*, doi:10.1016/j.jastp.2003.12.005.

Hertzog, A., et al. (2007), Stratéole/Vorcore—Long-duration, superpressure balloons to study the Antarctic lower stratosphere during the 2005 winter, *J. Atmos. Oceanic Technol.*, *24*, 2048–2061, doi:10.1175/2007JTECHA948.1.

Hertzog, A., G. Boccara, R. A. Vincent, F. Vial, and P. Cocquerez (2008), Estimation of gravity wave momentum flux and phase speeds from quasi-Lagrangian stratospheric balloon flights. Part II: Results from the Vorcore campaign in Antarctica, *J. Atmos. Sci.*, *65*, 3056–3070, doi:10.1175/2008JAS2710.1.

Hibbins, R. E., P. J. Espy, M. J. Jarvis, D. M. Riggin, and D. C. Fritts (2007), A climatology of tides and gravity wave variance in the MLT above Rothera, Antarctica obtained by MF radar, *J. Atmos. Sol. Terr. Phys.*, *69*, 578–588.

Hostetler, C. A., and C. S. Gardner (1990), Rayleigh lidar signal processing techniques for studies of stratospheric temperature structure and dynamics, *EOSL Pap. 90-003*, Univ. of Ill. at Urbana-Champaign, Champaign.

Innis, J. L., A. R. Klekociuk, R. J. Morris, A. P. Cunningham, A. D. Graham, and D. J. Murphy (2008), A study of the relationship between stratospheric gravity waves and polar mesospheric clouds at Davis Antarctica, *J. Geophys. Res.*, *113*, D14102, doi:10.1029/2007JD009031.

Kennedy, J. S. (1980), Comments on 'On detrending and smoothing random data' by A. J. Owens, *J. Geophys. Res.*, *85*(A1), 219–220, doi:10.1029/JA085iA01p00219.

Lighthill, J. (1978), *Waves in Fluids*, Cambridge Univ. Press, Cambridge, U. K.

Lindzen, R. S. (1981), Turbulence and stress owing to gravity wave and tidal breakdown, *J. Geophys. Res.*, *86*, 9707–9714, doi:10.1029/JC086iC10p09707.

Mitchell, N. J., L. Thomas, and A. K. P. Marsh (1990), Lidar studies of stratospheric gravity waves: A comparison of analysis techniques, *Ann. Geophys.*, *8*, 705–712.

O'Sullivan, D., and T. J. Dunkerton (1995), Generation of inertia–gravity waves in a simulated life cycle of baroclinic instability, *J. Atmos. Sci.*, *52*, 3695–3716.

Pfenninger, M., A. Z. Liu, G. C. Papem, and C. S. Gardner (1999), Gravity wave characteristics in the lower atmosphere at South Pole, *J. Geophys. Res.*, *104*, 5963–5984, doi:10.1029/98JD02705.

Plougonven, R., A. Hertzog, and H. Teitelbaum (2008), Observations and simulations of a large-amplitude mountain wave breaking over the Antarctic Peninsula, *J. Geophys. Res.*, *113*, D16113, doi:10.1029/2007JD009739.

Sato, K., and M. Yoshiki (2008), Gravity wave generation around the polar vortex in the stratosphere revealed by 3-hourly radiosonde observations at Syowa station, *J. Atmos. Sci.*, *65*, 3719–3735, doi:10.1175/2008JAS2539.1.

Senft, D. C., and C. S. Gardner (1991), Seasonal variability of gravity wave activity and spectra in the mesosphere region at Urbana, *J. Geophys. Res.*, *96*, 17,229–17,264, doi:10.1029/91JD01662.

Shibata, T., T. Fukuda, and M. Maeda (1986), Density fluctuations in the middle atmosphere over Fukuoka observed by an XeF Rayleigh lidar, *Geophys. Res. Lett.*, *13*, 1121–1124, doi:10.1029/GL013i011p01121.

Smith, S. A., D. C. Fritts, and T. E. VanZandt (1987), Evidence for a saturated spectrum of atmospheric gravity waves, *J. Atmos. Sci.*, *44*, 1404–1410, doi:10.1175/1520-0469(1987)044<1404:EFASSO>2.0.CO;2.

Taylor, M. J., E. H. Ryan, T. F. Tuan, and R. Edwards (1993), Evidence of preferential directions for gravity wave propagation due to wind filtering in the middle atmosphere, *J. Geophys. Res.*, *98*, 6047–6057, doi:10.1029/92JA02604.

Tsuda, T., M. Nishida, C. Rocken, and R. H. Ware (2000), A global morphology of gravity wave activity in the stratosphere revealed by the GPS occultation data (GPS/MET), *J. Geophys. Res.*, *105*, 7257–7274, doi:10.1029/1999JD901005.

Whiteway, J. A., and A. I. Carswell (1994), Rayleigh lidar observations of thermal structure and gravity wave activity in the high Arctic during a stratospheric warming, *J. Atmos. Sci.*, *51*, 3122–3136, doi:10.1175/1520-0469(1994)051<3122:RLOOTS>2.0.CO;2.

Whiteway, J. A., and T. J. Duck (1996), Evidence for critical level filtering of atmospheric gravity waves, *Geophys. Res. Lett.*, *23*, 145–148, doi:10.1029/95GL03784.

Whiteway, J. A., T. J. Duck, D. P. Donovan, J. C. Bird, S. R. Pal, and A. I. Carswell (1997), Measurements of gravity wave activity within and around the arctic stratospheric vortex, *Geophys. Res. Lett.*, *24*, 1387–1390, doi:10.1029/97GL01322.

Wilson, R., M. L. Chanin, and A. Hauchecorne (1991a), Gravity waves in the middle atmosphere observed by Rayleigh lidar 1. Case studies, *J. Geophys. Res.*, *96*, 5153–5167, doi:10.1029/90JD02231.

Wilson, R., M. L. Chanin, and A. Hauchecorne (1991b), Gravity waves in the middle atmosphere observed by Rayleigh lidar 2. Climatology, *J. Geophys. Res.*, *96*, 5169–5183, doi:10.1029/90JD02610.

Wu, D. L., and J. H. Jiang (2002), MLS observations of atmospheric gravity waves over Antarctica, *J. Geophys. Res.*, *107*(D24), 4773, doi:10.1029/2002JD002390.

Yoshiki, M., N. Kizu, and K. Sato (2004), Energy enhancements of gravity waves in the Antarctic lower stratosphere associated with variations in the polar vortex and tropospheric disturbances, *J. Geophys. Res.*, *109*, D23104, doi:10.1029/2004JD004870.

Zhang, F. (2004), Generation of mesoscale gravity waves in upper-tropospheric jet-front systems, *J. Atmos. Sci.*, *61*, 440–457.

X. Chu, W. Huang, and C. Yamashita, Cooperative Institute for Research in Environmental Sciences, University of Colorado at Boulder, 216 UCB, Boulder, CO 80309, USA.

P. J. Espy, Department of Physics, Norwegian University of Science and Technology, NO-7491 Trondheim, Norway.

H.-L. Liu, High Altitude Observatory, National Center for Atmospheric Research, Boulder, CO 80307-3000, USA.

G. J. Nott, Department of Physics and Atmospheric Science, Dalhousie University, Halifax, NS B3H 3J5, Canada.